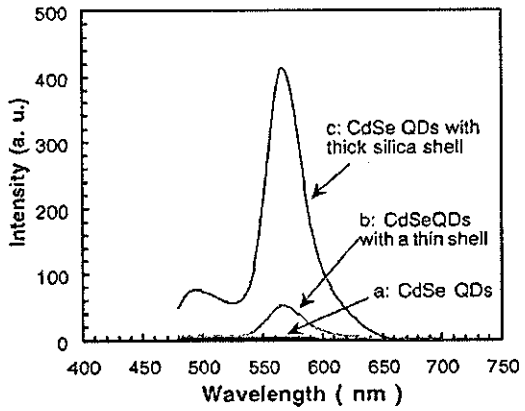

Fig. 3. Photoluminescence intensity (a.u.) of (a) CdSe QDs suspension; (b) CdSe QDs with a thin silica shell; (c) QDs with a thick silica shell. (λ_{exc} = 400 nm, $[Cd^{2+}]$ = 0.0006 M).

encapsulating (after being transferred to ethanol). Fig. 3 shows the improvement of the PL properties of the QDs in the coating process. Obviously, the PL intensity of the final QDs with a thick rigid shell of silica was much stronger than that of the initial QDs. The reason for the increased PL intensity is the formation of a thick silica shell, which may have a higher potential for the ground-state electron. This makes the shell of silica analogous to the CdS [14] and ZnS [16] around the CdSe core, the CdSe [17] shell around HgSe core, since CdSe semiconductor has a lower band gap than that of CdS, ZnS, and SiO_2, a higher band gap than that of HgSe. This conclusion is possibly further supported from the opposite side by the fact that formation of HgSe shell around CdSe core decreased the PL intensity of the CdSe nanoparticles [17], since the band gap of HgSe is lower than that of CdSe semiconductor.

Here, it has been found that the PL intensity increased after the addition of ethanol in the cases with different concentrations of MPS and/or different pH. That is to say, the PL intensity of the QDs with a thick shell of silica is always higher than that with a thin silica shell (before addition of ethanol). However, in comparison to the initial QDs, the PL intensity of MPS capped and then silica thinly coated CdSe QDs (before addition of ethanol) became weak at high pH or in the presence of high concentrated MPS. Virtually, the PL became undetectable at pH > 10 or with 10 times concentrated MPS of the current one. Rogach et al. [22] has obtained the similar results. Actually, it has been found that the existence of MPS negatively affected the PL intensity of the QDs. Then, the enhancement of silica shell on the PL intensity was so strong that the QDs exhibited a higher PL intensity than the initial QDs even after the formation of a thin shell of silica under the standard conditions, as revealed from Fig. 3. The details about the effect of MPS on PL will be shown elsewhere.

3.4. Stabilization against intense illumination

Fig. 4 shows the changes in PL intensity at different illumination times after exposure to Ar laser (532 nm, 700 mW). It was firstly found that the PL intensity of the bare CdSe QDs increased rapidly in the initial stage of the illumination. This seemed to result from the effect of photo annealing, and thereby, the defect sites on the surface of the QDs decreased. Then, under a long strong illuminating, the PL intensity greatly decreased. It can be considered that the QDs absorbed so many photons with a great energy and then decomposition into the elements Cd and Se took place under the extreme conditions. This has previously been pointed out by Spanhel et al. in the case of CdS [27].

However, in case of silica encapsulated CdSe QDs, the PL intensity was kept almost constant except the slightly increase in the quite early stage of the illumination. Probably, the silica shell was rigid

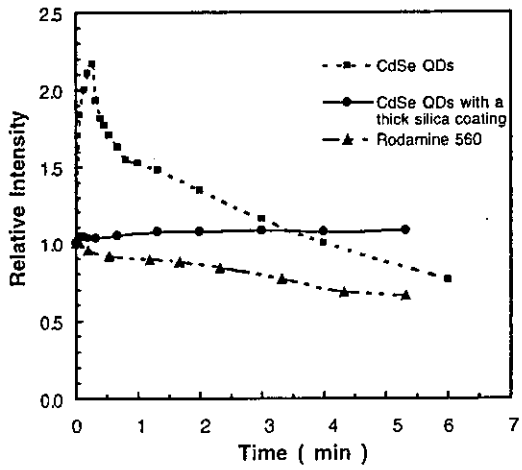

Fig. 4. Changes in photoluminescence intensity at different illumination (700 mW, Ar Laser) times. (a) CdSe QDs; (b) silica-encapsulated CdSe QDs; (c) Rhodamine 560.

enough to confine the Cd and Se atoms in the fixed space and site, and then the structure of CdSe QDs was maintained well. Furthermore, even the photo-stability of silica encapsulated CdSe QDs was stronger than that of the organic dye (Rhodamine 560) as the PL intensity of Rhodamine 560 gradually decreased under illuminating. This has also been confirmed for ZnS coated CdSe QDs [13].

4. Conclusions

Silica shell has produced around CdSe cores by a slow deposition of silica solute while being transferred to ethanol in the presence of MPS. The successful passivation of the surface states of colloidal CdSe QDs has been confirmed from the photo-oxidation and -illumination experiments and the TEM images. Moreover, the promotion of the photoluminescence intensity has been observed after passivating the CdSe cores.

Acknowledgement

The authors gratefully acknowledge Welfare Department of Japanese government for its support in research fund.

References

[1] D.L. Klein, R. Roth, A.K.L. Lim, A.P. Alivisatos, P.L. McEuen, Nature 389 (1997) 699.
[2] A. Henglein, Chem. Rev. 89 (1989) 1861.
[3] W.L. Wilson, P.F. Szajowski, L.E. Brus, Science 262 (1993) 1242.
[4] P. Mulvaney, L.M. Liz-Marzán, M. Giersig, T. Ung, J. Mater. Chem. 10 (2000) 1259.
[5] L.M. Liz-Marzán, M. Giersig, P. Mulvaney, Langmuir 12 (1996) 4329.
[6] T. Li, J. Moon, A.A. Morrone, J.J. Mecholsky, D.R. Talham, J.H. Adair, Langmuir 15 (1999) 4328.
[7] M.A. Correa-Duarte, M. Giersig, L.M. Liz-Marzán, Chem. Phys. Lett. 286 (1998) 497.
[8] C.B. Murray, D.J. Norris, M.G. Bawendi, J. Am. Chem. Soc. 115 (1993) 8706.
[9] J.E.B. Katari, V.L. Colvin, A.P. Alivisatos, J. Phys. Chem. 98 (1994) 4109.
[10] S. Gorer, G. Hodes, J. Phys. Chem. 98 (1994) 5338.
[11] E. Lifshitz, I. Dag, I. Litvin, G. Hodes, S. Gorer, R. Reisfeld, M. Zelner, H. Miuti, Chem. Phys. Lett. 288 (1998) 188.
[12] M. Bruchez Jr., M. Moronne, P. Gin, S. Weiss, A.P. Alivisatos, Science 281 (1998) 2013.
[13] W.C.W. Chan, S. Nie, Science 281 (1998) 2016.
[14] X. Peng, M.C. Schlamp, A.V. Kadanich, A.P. Alivisatos, J. Am. Chem. Soc. 119 (1997) 7019.
[15] S. Liu, H. Guo, Z. Zhang, R. Li, W. Chen, Z. Wang, Phys. E 8 (2000) 174.
[16] B.O. Dabbousi, J. Rodriguez-Viejo, F.V. Mikulec, J.R. Heine, H. Mattoussi, R. Ober, K.F. Jensen, M.G. Bawendi, J. Phys. Chem. B 101 (1997) 9463.
[17] L. Xu, K. Chen, J. Zhu, H. Chen, H. Huang, J. Xu, X. Huang, Superlattice Microstruct. 29 (2001) 67.
[18] S.K. Bera, S. Chaudhuri, R.P. Gupta, A.K. Pal, Thin Solid Films 382 (2001) 86.
[19] R.M. Langford, M.J. Lee, S.W. Wright, C.P. Judge, R.J. Chater, T.J. Tate, J. Electr. Mater. 30 (2001) 925.
[20] H. Karl, W. Hipp, I. Groβhans, B. Stritzker, Mater. Sci. Eng. C 19 (2002) 55.
[21] Y. Ma, M. Li, H.M. El-hair, Y. Zhang, L. Xu, X. Huang, K. Chen, Phys. E 15 (2002) 48–52.
[22] A.L. Rogach, D. Nagesha, J.W. Ostrander, M. Giersig, N.A. Kotov, Chem. Mater. 12 (2000) 2676.
[23] T. Dannhauser, M. O'Neil, K. Johansson, D. Whitten, G. McLendon, J. Phys. Chem. 90 (1986) 6074.
[24] M. Gao, S. Kirstein, H. Möhwald, J. Phys. Chem. B 102 (1998) 8360.
[25] D.V. Talapin, A.L. Rogach, I. Mekis, S. Haubold, A. Kornowski, M. Haase, H. Weller, Colloid Surface A: Physicochem. Eng. Aspects 202 (2002) 145.
[26] P. Reiss, S. Carayon, J. Bleuse, A. Pron, Synth. Met. 139 (2003) 649.
[27] L. Spanhel, M. Haase, H. Weller, A. Henglein, J. Am. Chem. Soc. 109 (1987) 5649.

journal

J. Am. Ceram. Soc., 87 [1] 166–69 (2004)

Oxygen-Deficient Anatase Precipitated from High-Temperature Plasma

Yoshikiyo Kato

Department of Material and Biological Chemistry, Yamagata University, Yamagata 990-8560, Japan

Hiroko Yokobayashi

Research Center for Higher Education, Tohoku University, Sendai 980-8576, Japan

Atsuo Kasuya

Center for Interdisciplinary Research, Tohoku University, Sendai 980-8578, Japan

Masahiro Kagawa* and Masashi Kawasaki

Institute for Materials Research, Tohoku University, Sendai 980-8577, Japan

Feeding atomized aqueous solutions containing $TiCl_4$ into an argon high-temperature inductively coupled plasma (ICP) resulted in the formation of mixtures of white and blue particles. The mixtures consisted of anatase and an extra phase of rutile. Adding oxygen to the ICP led to the production of a single phase of white anatase. The blue particles could be characterized as oxygen-deficient anatase. Electrophoretic mobility measurements indicated that Na^+ participated in determining the surface potential of the mixtures. The oxygen defects may provide the adsorption sites to Na^+.

I. Introduction

The high photocatalytic performance of titanium oxide under visible light has recently been achieved by doping nitrogen, carbon, and metal ions.[1–3] These dopings were performed by sputtering, combustion, and ionized cluster beam methods, respectively. Thus, various material processing techniques have contributed to the preparation of new materials.

A modification of spray pyrolysis with a high-temperature inductively coupled plasma (ICP) can be applied to the preparation of ultrafine oxide particles (the spray-ICP technique). In this method the liquid droplets completely decompose in the ICP to form a gas phase from which the oxide particles precipitate in a short time.

The properties of powders depend on particle shape, sizes and size distributions, additives, and defects, etc. With anatase, a particle size of 25–40 nm is optimum for high photocatalytic activities.[4] Metal ion doping affects the incident proton conversion efficiency of nanocrystalline electrodes.[5] Phosphates inhibit anatase from transforming to rutile by hindering the mobility of surface ions.[6]

In the present study, ultrafine particles of anatase have been prepared by the spray-ICP technique. Since liquid or suspension precursors were used, the anatase would occlude water. Phosphates, when co-precipitated, possibly affect the transformation to rutile. The anatase was obtained as mixtures of white and blue particles; the latter particles could be deficient in oxygen. Probably the oxygen defects determine the surface potential. These subjects will be clarified by X-ray diffraction, electron microscope observation, thermal analysis, diffuse reflectance spectroscopy, and electrophoretic mobility measurements.

II. Experimental Procedure

The solution and suspension precursors were prepared from $TiCl_4$ and H_3PO_4 (Wako Pure Chemicals) and distilled water. The solutions containing $TiCl_4$ (0.3 mol/L) were used to precipitate pure TiO_2. The suspensions as-prepared by mixing $TiCl_4$ and H_3PO_4 (0.1 mol/L nominal Ti concentration, 5 wt% H_3PO_4) were used to co-precipitate the phosphate. Figure 1 shows the experimental setup. The atomized precursor was introduced into an Ar-ICP (feed rate, 10–20 cm^3/h) through a narrow-tipped quartz nozzle (1.5–1.7-mm diameter) with an Ar carrier gas of 1.4 L/min. The ICP (40-mm diameter, 160-mm length) was generated at a frequency of 6 MHz and a running power of 5–6 kW and was stabilized with an Ar cooling gas of 30 L/min. The precipitation conditions were made oxidative by adding 6–8 mol% O_2 into the cooling gas. This required a running power of 7–8 kW. Introduction of the precursor generated a tail flame of 600 mm long. The particles were precipitated on the wall of a Pyrex glass tube (110-mm diameter and 600-mm length) placed under the ICP and also using an electrostatic precipitator connected to the glass tube. The particles were characterized by X-ray diffraction (XRD; Rigaku, Cu$K\alpha$ radiation with Ni filter and single graphite monochromator), transmission electron microscope observation (TEM; JEOL, JM3010), thermogravimetric and differential thermal analysis (TGA and DTA; Ulvac-Shinkuriko, MTS-9000, heating rate of 10°C/min, in air), diffuse reflectance spectroscopy (DRS: Hitachi, UV-spectrometer 330, integration sphere 210-2101, $BaSO_4$ sample holder of 3-mm diameter), and microscope electrophoresis (magnification, 150; dark field illumination; in 1×10^{-3} mol/L $NaClO_4$ or tetra-*n*-butylammonium perchlorate ($(n\text{-}Bu)_4NClO_4$) electrolytes; pH adjustment with $HClO_4$, NaOH, and/or $(n\text{-}Bu)_4NOH$ (Nacalai); particles were suspended around neutral pH).

III. Results and Discussion

Table I summarizes the colors and phases of the powders precipitated on the glass-tube wall and in the electrostatic precipitator.

R. H. French—contributing editor

Manuscript No. 10361. Received July 5, 2003; approved August 18, 2003.
*Member, American Ceramic Society.

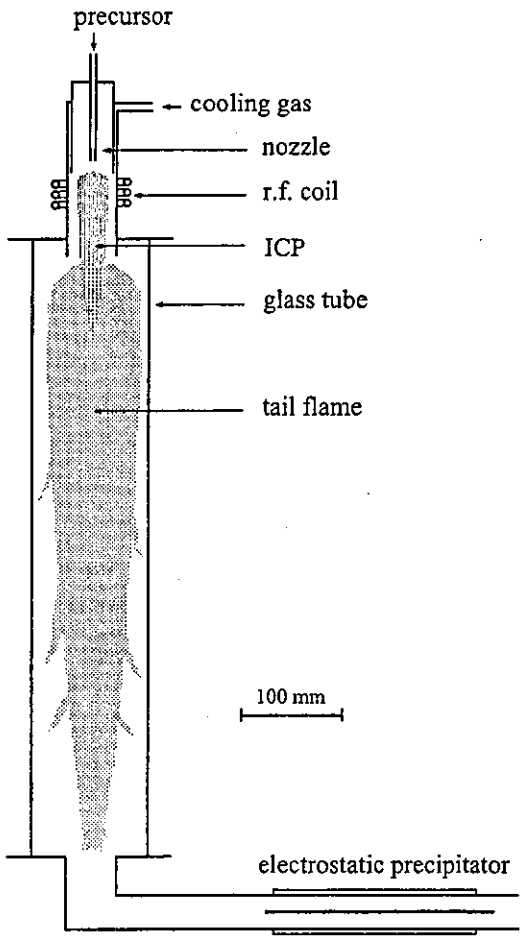

Fig. 1. Experimental setup.

The powder precipitated on the glass-tube wall from the Ar-ICP (experiment 1, Ar-g) contained white and blue particles (about 1:1 in volume ratio), whereas that precipitated in the electrostatic precipitator (Ar-e) held only white particles. XRD indicated that Ar-g and Ar-e both consisted of anatase and an extra phase of rutile (ratio in highest XRD peak; 101-anatase:110-rutile ≅ 6:1 for Ar-g and 14:1 for Ar-e). TEM revealed that Ar-g and Ar-e were composed of spherical particles. With the particle size, however, Ar-g had a wider particle size distribution (10–50 nm) than Ar-e (10–30 nm).

The precipitation from the oxidative conditions (experiment 2) resulted in the formation of white particles that were characterized as a single phase of anatase (O_2-g and O_2-e). Hence, the blue particles contained in Ar-g can be identified as oxygen-deficient anatase.

In the co-precipitation of the phosphate (experiment 3), P-g was obtained as a mixture of white and blue particles. Its phase was, however, only anatase. This differs from Ar-g. After all, the co-precipitation of the phosphate did not affect the oxygen deficiency but promoted the formation of anatase.

The particle size and phase of the powders depended on the precipitator. The particles may be roughly divided into two groups based on where and how they condense from the ICP. The first group is the particles condensed from the surface of the tail flame in the direction perpendicular to the flame axis, and the second group is those condensed at the flame tip. The glass-tube wall precipitates most of the particles of the first group, whereas the electrostatic precipitator traps those of the second group. The glass tube encloses the tail flame so close that part of the tail flame is rapidly cooled, resulting in the formation of small particles. In the tail flame, turbulence flows are inclined to occur. These flows are maintained at high temperatures for a long time. The particles involved in these flows grow large because the chance of coalescence is high. Additionally, the succeeding crystal growth is often promoted, accompanying the formation of a high-temperature form of isomorphs, i.e., rutile. After all, with the powders precipitated on the glass-tube wall, the particle size distributes in a wide range and the content of rutile becomes high. At the tail flame tip, the particles condense under relatively homogeneous precipitation conditions, and they are carried away to the electrostatic precipitator immediately after the condensation. This leads to the formation of particles with a narrow particle size distribution.

The blue particles were contained only in the powders precipitated on the glass-tube wall (Ar-g and P-g), implying that they were formed by rapid quenching of the tail flame. Probably their crystal growth ceased before the stoichiometric composition of anatase was formed. Under the oxidative precipitation conditions, the stoichiometric composition could be achieved because of the high concentration of oxygen (O_2-e and O_2-g).

Figure 2 shows TGA and DTA of Ar-g before (a) and after (b) being dried at room temperature. Before being dried, Ar-g exhibited two large weight loss steps in the temperature range up to about 500°C. Since the aqueous precursors were used, Ar-g occludes water. The first step is assigned to the release of the water adsorbed on the particle surface, and the second one is to that of the water staying in the lattice. Above 600°C a small amount of weight gain occurred. When Ar-g was quenched at 450°C, its color was found to have already changed from blue to yellow. Clearly the oxygen defects were partly filled. Consequently, the weight gain above 600°C is due to the uptake of oxygen. Reasonably, the dried Ar-g revealed a smaller weight loss below 500°C, so a larger amount of weight gain above 530°C resulted. The main DTA profile corresponded to the endothermic and exothermic reactions of the water releases and oxygen uptake. The noiselike profile suggests that the particles are so small that they move in the DTA cell.

TGA revealed a plateau in the temperature range of 430°–530°C (Fig. 2(a)). Apparently Ar-g contains 4.1% (=2.0 + 2.1) water and 0.7% oxygen deficiency. The previously dried Ar-g is expected to exhibit 0.72% (=0.7 × 100/95.9) oxygen uptake. However, the apparent uptake was 2.5% (Fig. 2(b)), which is much larger than the expected weight increase. This discrepancy can be explained in terms of duplication of weight loss and gain. That is, the releases of water and the oxygen uptake occur simultaneously in the plateau temperature range. As cited above, the color change of Ar-g quenched at 450°C supports the occurrence of the oxygen uptake.

The transformation of anatase to rutile increased with increasing temperature. At 450°C the rutile content against anatase in the XRD peak intensity was found to have already increased, and at 1050°C the complete conversion to rutile was ascertained. The co-precipitation of the phosphate hindered this transformation. The anatase of P-g was retained up to nearly 1000°C. Mechanically mixed phosphates cannot retain anatase at such high temperatures, and only the phosphate chemisorbed on TiO_2 as a bidentate ligand can block the transformation by inhibiting the surface ion mobility.[6] The phosphate in the present study is likely to stabilize the anatase through the same mechanism. In other words, the phosphate settles on the particle surface in the precipitation process. On the oxygen uptake, however, the phosphate had no effect. P-g changed to white when heated for 15 min at 400°C.

Figure 3 shows the DRS of Ar-g (a), Ar-g quenched at 450° (b) and at 1050°C (c), and commercial anatase quenched at 1050°C (d). Ar-g had two absorption bands, one at 450–500 nm and the other above 500 nm. The absorption edge was around 390 nm, which is almost equal to that of ordinary anatase. At 450°C, the bands weakened and the absorption edge red-shifted. At 1050°C, the absorption edge red-shifted further to 415 nm and the two bands almost disappeared. The absorption edge was almost the same as that of the commercial anatase quenched at 1050°C. However, the former was light yellow, whereas the latter was white. The oxygen uptake of Ar-g was not completed even at 1050°C. This is reflected in their DRS spectra. Ar-g quenched at 1050°C had a continuous weak absorption band above 400 nm,

Table I. Colors and Phases of Powders Precipitated on the Glass Tube Wall (Glass) and in Electrostatic Precipitator (Electrostatic)

Experiment	Precursor	Cooling gas	Colors and phases†	
			Glass	Electrostatic
1	$TiCl_4$	Ar	Blue + white (Ar-g), anatase + rutile	White (Ar-e), anatase + rutile
2	$TiCl_4$	Ar + O_2	White (O_2-g), anatase	White (O_2-e), anatase
3	$TiCl_4$ + H_3PO_4	Ar	Blue + white (P-g), anatase	White (P-e), anatase

†Parentheses indicate names of powders used in text.

whereas the commercial anatase quenched at the same temperature revealed no absorption band there.

Figure 4 shows the mobility (U; $(\mu m \cdot s^{-1})/(V \cdot cm^{-1})$) vs pH of O_2-e (a) and Ar-g (b) measured in the $NaClO_4$ electrolyte, and Ar-g measured in the $(n\text{-}Bu)_4NOH$ electrolyte (c). In the $NaClO_4$ electrolyte, as pH increased, the mobility of O_2-e shifted gradually in the negative direction, having an isoelectric point (iep) at pH 6. This iep was almost equal to reported values,[7,8] implying that O_2-e is an ordinary defect-free anatase. The mobility of Ar-g exhibited a yoyo-ing pH dependence with a positive shift between pH 6 and 10. This shift did not appear in the $(n\text{-}Bu)_4NClO_4$ electrolyte. Reasonably Na^+ causes the positive shift. Since Ar-g contains the blue particles that have oxygen defects, Na^+ is likely to interact with the defects and determine the particle surface.

We will describe the mobility vs pH of Ar-g measured in the $NaClO_4$ electrolyte in terms of the surface charge density based on a simplified model of Ref. 9. At the solid liquid interface, protons are bound to negatively charged metal oxide ions (A^-) to provide positive sites (AH_2^+) in the high-pH region. With increasing pH, AH_2^+ dissociates stepwise to give neutral (AH) and negative sites, A^-. There must be the following equilibrium relations among these sites:

$$AH_2^+ \overset{K_+}{\rightleftharpoons} AH + H^+ \tag{1}$$

$$AH \overset{K_-}{\rightleftharpoons} A^- + H^+ \tag{2}$$

The respective dissociation constants for Eqs. (1) and (2), K_+ and K_-, are given by Eqs. (3) and (4):

$$K_+ = \frac{[AH]_{sf}[H^+]}{[AH_2^+]_{sf}} \tag{3}$$

$$K_- = \frac{[A^-]_{sf}[H^+]}{[AH]_{sf}} \tag{4}$$

where the square brackets with a suffix of "sf" represent the surface concentrations of the species involved per unit area at the interface. $[H^+]$ is the concentration of the proton in the solution.

Further, Ar-g has the oxygen defects that are equilibrated with Na^+:

$$A^* + Na^+ \overset{K'}{\rightleftharpoons} A^*{\cdot}Na^+ \tag{5}$$

where A^* represents the oxygen defect sites in equilibrium with Na^+. K' is an association constant given by

$$K' = \frac{[A^*{\cdot}Na^+]_{sf}}{[A^*]_{sf}[Na^+]} \tag{6}$$

where $[Na^+]$ is the concentration of Na^+ in the solution.

The total site arising from Eqs. (1) and (2) is c_1, and that from Eq. (5) is c_2,

$$c_1 = [AH_2^+]_{sf} + [AH]_{sf} + [A^-]_{sf} \tag{7}$$

$$c_2 = [A^*]_{sf} + [A^*{\cdot}Na^+]_{sf} \tag{8}$$

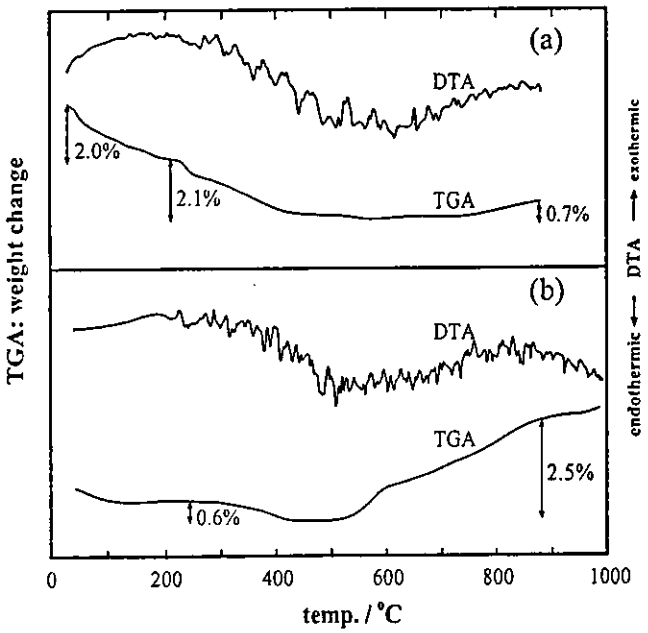

Fig. 2. TGA and DTA of Ar-g before (a) and after (b) being dried.

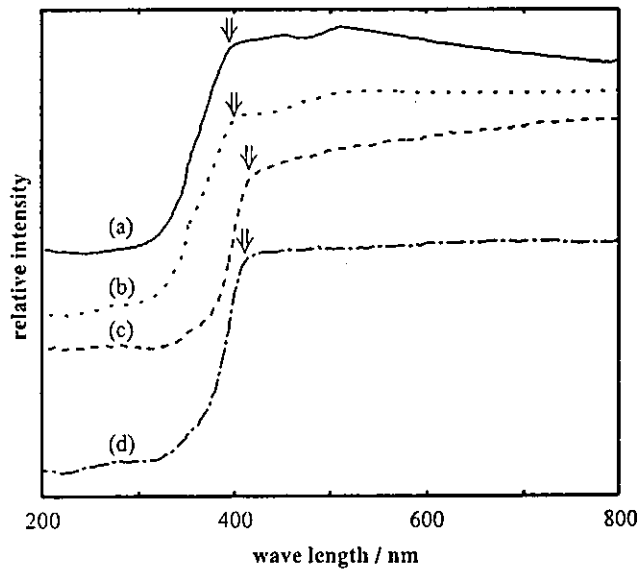

Fig. 3. DRS of Ar-g (a), Ar-g quenched at 450° (b) and at 1050°C (c), and commercial anatase quenched at 1050°C (d). ⇓ indicates the absorption edge.

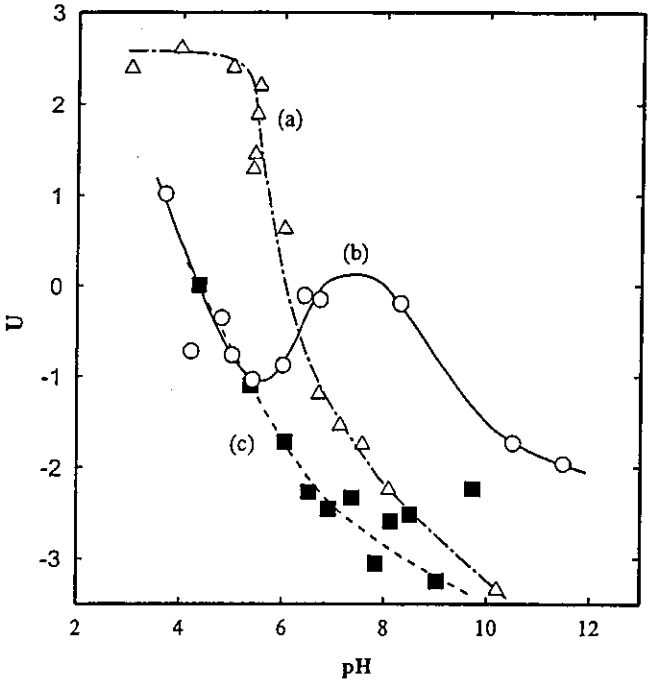

Fig. 4. U vs pH of O_2-e measured in $NaClO_4$ (a), of Ar-g in $NaClO_4$ (b), and of Ar-g in $(n\text{-Bu})_4NOH$ electrolyte (c).

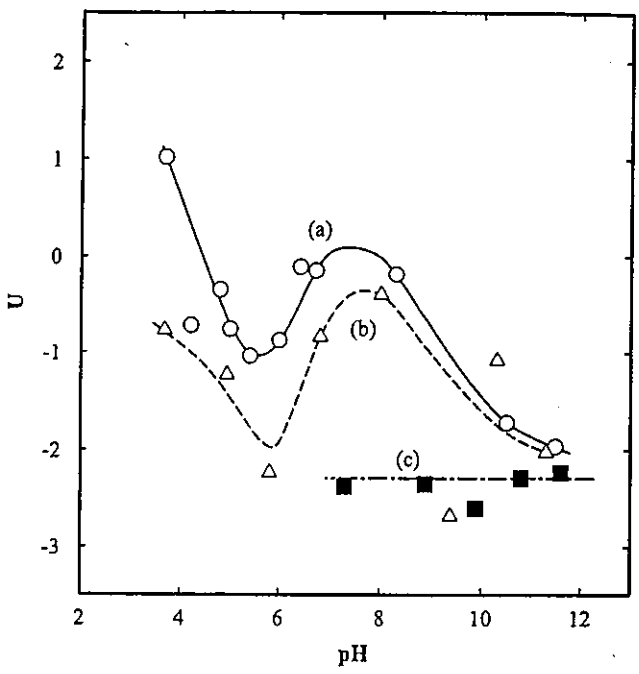

Fig. 5. U vs pH measured in $NaClO_4$: Ar-g (a), Ar-g after being water-washed (b), and Ar-g after being dispersed into NaOH (c).

in all, the surface charge density, σ, can be represented by

$$\sigma = [AH_2^+]_{sf} + [A^{*}\cdot Na^+]_{sf} - [A^-]_{sf}$$

$$= \frac{c_1}{1 + \frac{K_+}{[H^+]} + \frac{K_+K_-}{[H^+]^2}} + \frac{c_2}{\frac{[H^+]}{K'K_W} + 1} - \frac{c_1}{\frac{[H^+]^2}{K_+K_-} + \frac{[H^+]}{K_-} + 1} \quad (9)$$

where K_W is the ion product for water ($[H^+][OH^-] = 10^{-14}$).

Since the mobility is a function of the surface charge density, the mobility vs pH can be explained in terms of the dependence of σ on $[H^+]$ in Eq. (9). The mobility took a positive value at pH 4. As pH increased, the mobility decreased and shifted in the positive direction between pH 6 and 10. This finding indicates that there must be the following relation among the equilibrium constants.

$$K_+ > \frac{1}{K'K_W} > K_- \quad (10)$$

The values roughly estimated from curve fitting were as follows: K_+, in the order of 10^{-4}; K', 10^8; and K_-, 10^{-10}; $c_1{:}c_2 \cong 2{:}1$. The high K' value indicates that the oxygen defects have a strong affinity to Na^+.

Figure 5 shows the effect of some treatments for Ar-g on the mobility vs pH measured in the $NaCl_4$ electrolyte: Ar-g (a), Ar-g after being water-washed (b), and Ar-g after being dispersed in a NaOH solution of pH = 12 (c). The positive mobility shift observed between pH 6 and 10 could still be seen even after the specimen was water-washed. However, the shift did not appear on dispersion into the NaOH solution, indicating that the reverse reaction in Eq. (5) becomes slow. Thus, the oxygen defects interact with Na^+, and under certain conditions the Na^+ can firmly be held in the anatase.

IV. Summary

The titanium oxide powders prepared by the spray-ICP technique were composed of white and blue particles; the latter particles were characterized as oxygen-deficient anatase. On heating, the powders absorbed oxygen with the red-shift of the absorption edge and also with the transformation to rutile. In solutions containing Na^+, the oxygen defects provide adsorption sites to Na^+, participating in determining the surface potential.

Acknowledgments

The authors wish to thank Emeritus Professor of Tohoku University, Dr. S. Usui, for many helpful discussions.

References

[1]R. Asahi, T. Morikawa, T. Ohwaki, K. Aoki, and Y. Taga, "Visible Light Photocatalysis in Nitrogen-Doped Titanium Oxides," *Science (Washington, D.C.)*, 293, 269–71 (2001).

[2]S. U. M. Khan, M. Al-Shahry, and W. B. Inger Jr., "Efficient Photochemical Water Splitting by a Chemically Modified n-TiO_2," *Science (Washington, D.C.)*, 297, 2243–45 (2002).

[3]H. Yamashita, M. Harada, J. Misaka, M. Takeuchi, Y. Ichihashi, F. Goto, M. Ishida, T. Sasaki, and M. Anpo, "Application of Ion Beam Techniques for Preparation of Metal Ion-Implanted TiO_2 Thin Film Photocatalyst Available under Visible Light Irradiation: Metal Ion-Implantation and Ionized Cluster Beam Method," *J. Synchrotron Radiat.*, 8, 569–71 (2001).

[4]C. B. Almquist and P. Biswas, "Role of Synthesis Method and Particle Size of Nanostructured TiO_2 on Its Photoactivity," *J. Catal.*, 212 [2] 145–56 (2002).

[5]Y. Wang, H. Cheng, Y. Hao, J. Ma, W. Li, and S. Cai, "Photoelectrochemical Properties of Metal-Ion-Doped TiO_2 Nanocrystalline Electrodes," *Thin Solid Films*, 349, 120–25 (1999).

[6]J. Criado and C. Real, "Mechanism of the Inhibiting Effect of Phosphate on the Anatase → Rutile Transformation Induced by Thermal and Mechanical Treatment of TiO_2," *J. Chem. Soc., Faraday Trans. 1*, 79, 2765–71 (1983).

[7]M. M. Soltys, Z. M. Yaremko, N. H. Tkachenko, and V. D. Havryliv, "Poly-(methacrylic acid) Adsorption and Electrical Surface Properties of Titanium Dioxide Suspensions," *Adsorpt. Sci. Technol.*, 20 [7] 633–45 (2002).

[8]G. R. Wiese and T. W. Healy, "Adsorption of Al(III) at the TiO_2–H_2O Interface," *J. Colloid Interface Sci.*, 51 [3] 434–42 (1975).

[9]D. E. Yates, S. Levine, and T. W. Healy, "Site-Binding Model of the Electrical Double Layer at the Oxide/Water Interface," *J. Chem. Soc., Faraday Trans. 1*, 70, 1807–18 (1977). □

生物物理 44 (2), 75-80 (2004)

総説

キネシンの運動解析から見えてきた熱ラチェットメカニズム

京都大学大学院理学研究科化学専攻　西山雅祥
東北大学大学院工学研究科金属工学専攻　樋口秀男

Kinesin is an ATP-driven molecular motor that moves processively along a microtubule in a stepwise manner. The steps occur not only in the forward direction, but also in the backward. Here, we have studied the bidirectional stepping mechanism of kinesin motors. The stepping mechanism of the forward and backward movements was well characterized by Feynman's thermal ratchet model. The driving force of the stepwise movement is essentially Brownian motion, but it is biased in the forward direction by utilizing the free energy released from the hydrolysis of ATP.

kinesin / single molecule detection / Feynman's thermal ratchet model / loose coupling mechanism

1. はじめに

キネシン分子とは, Valeらによってイカの巨大な神経軸索から小胞輸送の担い手として同定された代表的な分子モーターである[1),2)]. キネシンには, 約350のアミノ酸からなる「モータードメイン」と呼ばれる部位が2つある. モータードメインには, ATPの加水分解反応を触媒する酵素活性と, 微小管への結合能があるため, ATPのもつ化学エネルギーを力学エネルギーに変換する役割があると考えられている.

キネシンは1分子でも微小管から解離することなく, 長距離（~1 μm）にわたってプラス端方向に運動することが可能であり, その滑り運動は8 nmを単位とするステップ状の変位から構成されている[3)-5)]. また, 高負荷条件下では, キネシンは, 時折, マイナス端方向への「バックステップ」を行うことも多くの研究者により観測されていた. ところが, 従来までの運動解析では, ステップ状の変位が見えない変位トレースをもとにした研究が主流であり, 出現頻度の少ないバックステップの影響はほとんど考慮されてこなかった. それに対して, 筆者らは, これまで見過ごされてきたバックステップにこそ, キネシンのステップ生成メカニズムを解く鍵が隠されていると考え, ステップの方向性を考慮したキネシンの運動解析を行った. 本稿では, キネシンの運動解析から見えてきた, 熱ゆらぎから一方向性の滑り運動をとりだすファインマン型の熱ラチェット機構に関して解説を行う.

2. キネシン1分子のナノメートル計測と運動解析

2.1 暗視野型1分子ナノメートル計測法の開発

従来までの光ピンセットを用いたナノメートル計測法では, 10 nm程度の大きさしかないモータードメインに対してきわめて大きなビーズ（直径1 μm程度のポリスチレン球）を目印として用いていた（本文のフォントを10 nmとすると, 紙面の横幅が1 μm程度となる）. 大きなビーズは, 光学顕微鏡下でその像を容易に検出できる反面, 水溶液中で大きな粘性抵抗を受けることになり, 時間応答能の制約を受けてしまう. そこで, 筆者らは, 直径0.2 μmの小さなビーズを用いた分解能の高い1分子ナノメートル計測法の開発に取り組んだ. 開発当初, 明視野型や微分干渉型などの結像系を試みたものの, 小さなビーズから鮮明な像を得ることはできなかった. そこで, バクテリアの鞭毛モーターの高速回転運動の検出に利用されていた斜光暗視野照明法を導入し[6)], 小さなビーズから明瞭で十分な光強度をもつ暗

Feynman's Thermal Ratchet Mechanism on Kinesin Motors
Masayoshi NISHIYAMA* and Hideo HIGUCHI**
* Department of Chemistry, Graduate School of Science, Kyoto University
**Department of Metallurgy, Graduate School of Engineering, Tohoku University

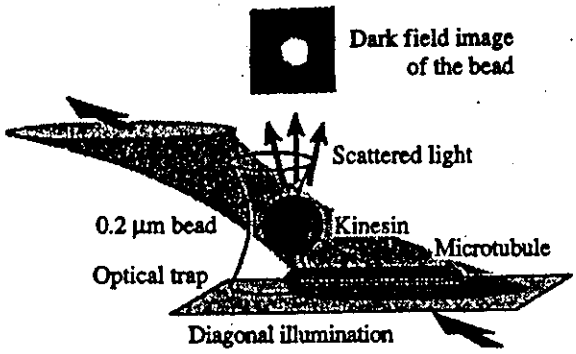

Fig.1 Dark-field style laser trapping nanometry. Single kinesin molecules were attached to a bead captured by an optical trap and brought into contact with a microtubule attached to a glass surface. The bead was illuminated diagonally by a focused red laser and its dark field image was projected onto a quadrant photodiode. The displacement of the bead was determined by measuring the differential output of the quadrant photodiode with nanometer accuracy.

視野像をとりだすことに成功した[5),7)].

筆者らが開発した暗視野型1分子ナノメートル計測法の概念図を示す（Fig.1）．ビーズ上のキネシンが，微小管に沿って滑り運動を開始すると，ビーズも分子の動きに追随する．ビーズは集光したレーザー光で照明されており，その散乱光は四分割光ダイオード上に投影されている．したがって，キネシン分子の動きは，光ダイオード上の暗視野像の動きとして計測されることになる．ナノメートルの位置分解能は，光ピンセットでビーズを捕捉し，その熱ゆらぎを抑制することで達成される．この暗視野型の1分子ナノメートル計測法によって，筆者らは，生理環境に近い条件下（高ATP濃度かつ無負荷）の変位トレースから，キネシンの8 nmステップを初めて検出できた[8)]（Fig.2a）．この測定系を用いると，キネシンのステップ状変位を最高で20 μsの時間分解能で計測可能となり（分子モーターの変位計測としては世界最高の分解能），その結果，8 nmステップの立ち上がり部分から，2つの連続した4 nmサブステップを検出することにも成功している[5),7)].

2.2 キネシンはATPを加水分解するごとに前か後ろにステップする

キネシンの変位トレースは，おおむね，前方向（微小管のプラス端）へのステップ状変位から構成されているものの，時折，後ろ方向（マイナス端）への運動（バックステップや微小管からの解離）も見られた（Fig.2b）．筆者らは，変位トレースの全負荷領域にわたって，ステップ状の変位が明瞭に検出されているものを選び出し，

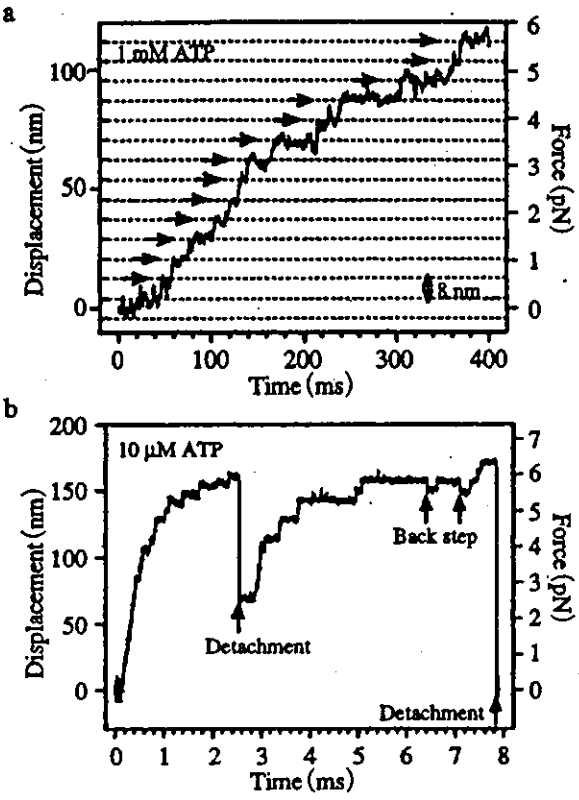

Fig.2 Stepwise movements caused by single kinesin molecules. (a and b) Time courses of the displacements of single kinesin molecules. [ATP] = 1 mM (a) and 10 μM (b). The displacement of kinesin was obtained from the bead displacement taking into consideration the compliance of the experimental system. The force was calculated from the displacement and trap stiffness.

次に，各ステップの負荷の大きさ，運動の方向性，ステップの時間間隔（dwell time）を1つ1つ丹念に調べあげた．運動の方向性は，前方向への8 nmステップを前進運動，バックステップや微小管からの解離を後退運動として解析した[8)]．Fig.3aは，ATP濃度1 mMの変位トレースから，各負荷領域における前進運動と後退運動の数を数え，それぞれの割合をプロットしたものである．後退運動の出現頻度は，低負荷領域（<4 pN）では，数%にも満たないが，負荷の増大とともに増加し，7-8 pNの負荷領域では，後退運動と前進運動の割合は同程度となった．低いATP濃度（10 μM）の変位トレースからも同じような前進後退運動の負荷依存性が得られているので，運動の方向性はATPの結合反応と無関係に決まることになる．

キネシンのステップ状変位とATPの加水分解反応との対応関係を調べるため，キネシンが前進運動，または後退運動を行うまでの時間間隔（dwell time）を解析した．Fig.3bは，キネシンが前進するまでのdwell timeの平均値を負荷に対してプロットしたものである．dwell

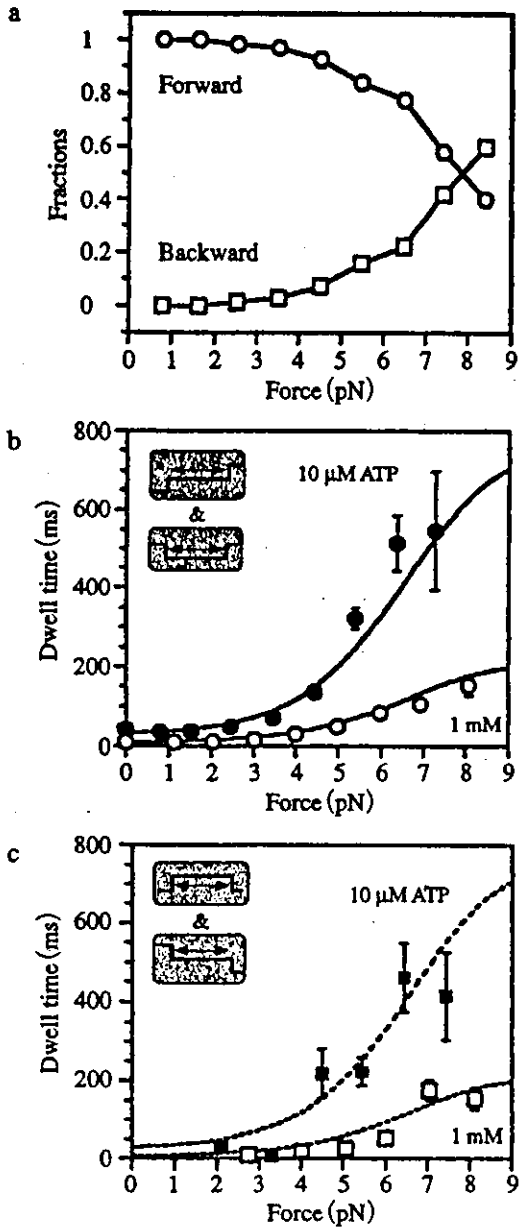

Fig.3 Analysis of the forward and backward movements. (a) Ratio of the forward (○) and backward (□) movements at 1 mM ATP. (b) Dwell time before the forward movement. 1 mM (○) and 10 μM (●) ATP. (c) Dwell time before the backward movement. 1 mM (□) and 10 μM (■).

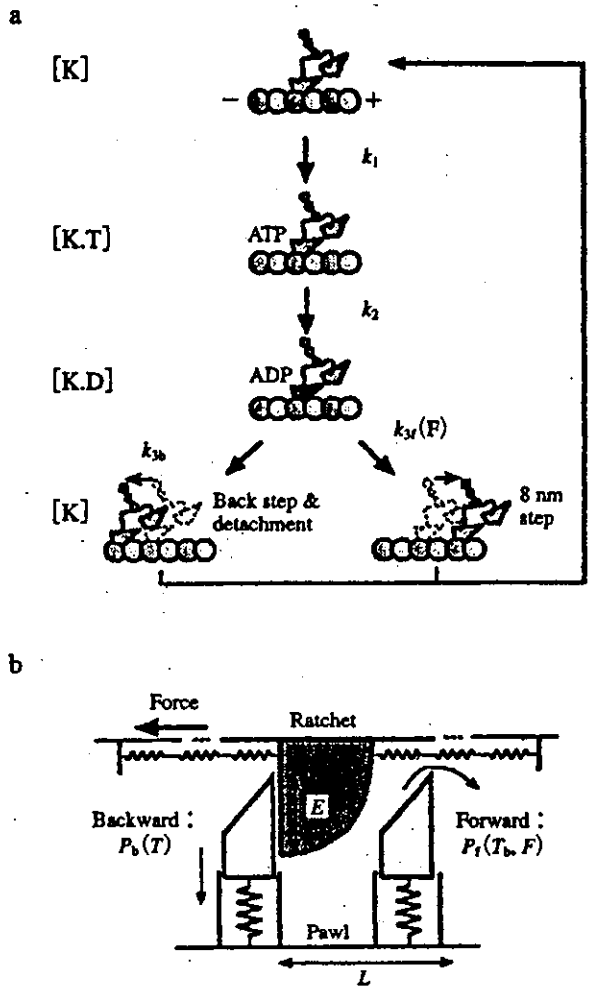

Fig.4 Stepping kinetics of the bi-directional movement. (a) Branched kinetic pathway. Kinesin attached to the microtubule with one motor-domain [K]. The ATP molecule binds to the head [K.T] and is hydrolyzed [K.D]. After kinesin moves either to the forward or backward direction, the ADP molecules are released [K]. (b) Feynman's thermal ratchet model.

timeは，高負荷条件下や低ATP濃度下において長くなることが明らかになった．この結果は，キネシンの滑り速度の負荷依存性やATP濃度依存性を調べた過去の報告例と一致した[4]．次に，後退運動までのdwell timeを解析したところ，前進運動の場合と同様の負荷依存性，ATP濃度依存性をもつことがわかった．これは，キネシンは，後ろに戻るときもATPの加水分解反応を必要とし，また，大きな負荷が加わるほど後ろに戻りにくくなるという性質をもつことを意味している．この興味深い実験結果は，従来のタイトカップリング型の運動モデル（ATP加水分解反応が，必ず8 nmステップに共役する）では説明することはできない．

そこで，筆者らは，両方向性の運動に関する一連の実験結果を説明するため，「キネシンはATPを加水分解した後，前か後ろのどちらかに運動する」というモデルを考案した（Fig.4a）．エネルギー入力であるATPの加水分解反応が，常に前方向への8 nmステップに共役しているわけではないので，このモデルは，ルースカップリング型の化学ー力学エネルギー共役関係となる．キネシンの前進運動と後退運動は，同一状態から競合的に発生するので，反応経路は分岐することになる．分岐

点でのキネティクスを考えると，前進運動と後退運動の生成確率は，$k_{3f}/(k_{3f}+k_{3b})$ と $k_{3b}/(k_{3f}+k_{3b})$，また，両者の生成速度はともに $k_{3f}+k_{3b}$ となる．この三状態モデルを用いて，運動の方向性（Fig.3a）とステップの時間間隔（Fig.3b）の解析を行い，各反応速度を決定した（詳しい過程は省略）[8]．その結果，意外にも，前進運動の反応速度（k_{3f}）のみが負荷に依存し，後退運動の反応速度（k_{3b}）は負荷と独立であることが明らかになった（Fig.5）．この k_{3f} と k_{3b} における非対称な負荷依存性は，ファインマンの熱ラチェットにおいて見られる前進後退運動の負荷特性と一致する．次章では，議論を k_{3f} と k_{3b} に絞り，方向性のない熱運動から一方向性の滑り運動を生み出す仕組みについて解説を行う（k_1, k_2 は，熱ラチェットによる滑り運動の発生過程とは関係がないので無視する）．

3. ATP駆動型分子モーターと熱ラチェット機構

3.1 ファインマンの熱ラチェット

大沢はルースカップリングを実現しうる分子メカニズムとして，ファインマンの熱ラチェットを導入した[9),10)]．ファインマンの熱ラチェットのエッセンスは，非対称な形をした爪と歯止めに「温度差」をもうけることで，方向性のない熱ゆらぎから方向性のある滑り運動を発生できる点にある．本稿では，爪（ratchet）を分子モーター（キネシン），歯止め（pawl）の列を微小管に対応させ，爪の温度を T_f，歯止めの温度を実験時の温度 T（＝298 K）として議論を進める．

Fig.4b は爪と歯止めの模式図であり，分子モーターの進む向き（前向き，キネシン－微小管系では微小管のプラス端方向）が，右になるように描いてある．爪は水平方向，歯止めは垂直方向にのみゆらぐことが可能で，爪の円形斜面が歯止めの斜面に面している．爪が前方向に1コマ進むためには，爪の円形斜面で歯止めを押し下げる仕事 E と，負荷 F に抗して距離 L を進むための仕事を行う必要がある．そのために必要なエネルギーは，温度 T_f の熱浴から借りなければならない．それに対して，後ろ方向に進むためには，構造上の制約により爪は歯止めを押し下げることができないので，温度 T の熱浴からエネルギーを借りて歯止めを引っ込める必要がある．したがって，爪が前向き，または，後ろ向きに動く確率はボルツマン分布にしたがい，それぞれ

$$\exp(-(E+FL)/k_BT_f) \qquad (1)$$

$$\exp(-E/k_BT) \qquad (2)$$

に比例する．ここで，E は障壁の高さ，F は負荷の大きさ，L はステップサイズとなる．

第1の特徴として，温度 T_f と T の「温度差」によって，前後に動く確率が調節されている点が挙げられる（Arrhenius/Eyring 型の反応速度論では，温度を一定にとり，障壁の高さで反応速度（確率）の大小関係が議論される）．爪と歯止めの間に「温度差」がない場合は，前後に動く確率は同じであり（無負荷時），一方向性の運動は生まれない．第2の特徴は，爪が前に動く確率だけが，負荷の影響を直接受けている点にある．このモデルでは，負荷の感受性パラメーターとして，爪の1コマ当たりの変位量（L）を採用しているので，負荷に対して行う仕事（FL）が，確率の変化に明瞭に組み込まれている．この爪の1コマ当たりの変位量は，キネシン－微小管系の場合では，微小管の構成単位であるチューブリンダイマーの長さに相当する（ステップサイズとも一致）．

今日に至るまで，熱ゆらぎから一方向性の滑り運動をとりだすさまざまな仕掛けが発表されているが[11]，ファインマンの熱ラチェットモデルはその先駆けとも言える存在である．このモデルの特徴は，一方向性の運動機能を爪と歯止めの形や「高温」状態に集約させることで，エネルギー論として物理の問題がどこにあるのかをはっきりとさせている点にある．

3.2 ATP駆動型分子モーターの運動解析

大沢らは，ファインマンの爪と歯止めの「温度差」を $T_f/T=3$-4 と仮定すると，筋肉の収縮過程をうまく説明できることを見いだした[9]．筋繊維を用いた当時の実験結果には，爪と歯止めが生み出す個々のステップは検出されておらず，あくまでモデル解析の域をでなかった．

それに対して，筆者らは，ファインマンの熱ラチェットに見られた反応速度の非対称な負荷依存性を，キネシンのステップ状変位の運動解析から実証することに

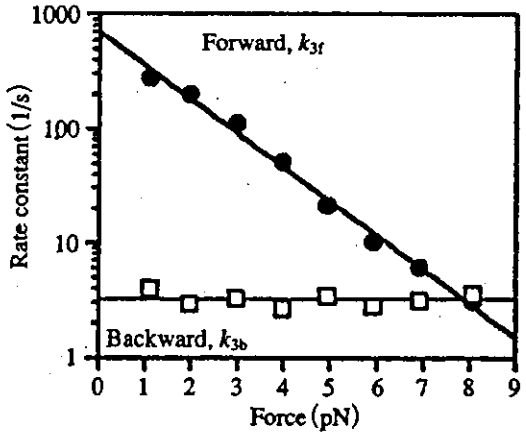

Fig.5 Load dependence of the rate constants of k_{3f} and k_{3b}.

成功している．キネシンが前に進む際の反応速度（k_{3f}）は負荷に依存するが，後ろに進む反応速度（k_{3b}）は負荷とは独立であったので（Fig.5），式（1）（2）を用いて解析を行った．その結果，爪の温度は$T_f = 2.8T$（～830 K）で，障壁の高さは$E = 8.4\ k_BT$に対応することが明らかになった[8),12)]．これは，ファインマンの熱ラチェットに対応する現象が，生体分子のダイナミクスから実験的に見いだされた世界で初めての事例であると思われる．

次に，筆者らは同様の解析手法を用いて，ほかの分子モーターである*Tetrahymena*繊毛の22Sダイニン，*Chlamydomonas*軸糸の内腕ダイニンC，ミオシンVの運動解析を行った．これらの分子モーターでは，その最大力や力－速度関係などの力学的な性質は一致していないにもかかわらず，その滑り速度の負荷依存性は，キネシンと同様に爪の温度を歯止めの約3倍とするモデルで説明されることが判明した[12)]．これまでのX線結晶構造解析により，キネシンと骨格筋ミオシンの一部とは構造が似ており，さらに，ヌクレオチド結合部位周辺の構造は，情報伝達分子であるGタンパク質ともよく似ていることが明らかにされている．ATP駆動型分子モーターにとっての「温度差」とは，ATPを加水分解するメカニズムの共通性や，分子が利用できる自由エネルギー値の共通性の表れと考えられる．

分子間で共通性が見られた「温度差」に対して，障壁の高さEには，分子種により大きな違いがみられた．キネシンやミオシンVの場合では，障壁の値が大きく（E～$8\ k_BT$），爪の滑り速度は遅いものの，誤作動（後退運動）を生じる危険性は小さくなる傾向が見られた（障壁を高めるとタイトカップリングになる）．これらの分子は，細胞内でも原則として1分子で駆動しているため，外的な要因に惑わされず，正確に駆動できるように設計されているのであろう．その反対に，内腕ダイニンCの障壁は小さな値を示しており（$E = 1.6\ k_BT$），これは分子単体としては誤作動の頻度が高いことを意味している．しかしながら，障壁が低いと，周囲の分子の動きに自らを同調させることも容易となり，分子集団として高度な機能を生み出すことも可能となる．また，この障壁の高さは，爪と歯止めの温度差が$T_f/T = 3$の条件では，最も速い滑り速度を達成できる点も見逃せない．内腕ダイニンCは，ほかの分子と協調してリズミカルなべん毛運動を達成するために，高度に進化した分子モーターかもしれない．

以上，ファインマンの熱ラチェットを用いて，ATP駆動型分子モーターの運動解析を行ってきた．分子モーターは，一方向性の滑り運動を生み出す源となる「温度差」には共通性を保持し，分子間の相互作用力ともいえる「障壁」には多様性をもたせていることが簡潔に示されたといえよう[13)]．

4. 熱ゆらぎから仕事を取り出す仕組み

ここでは，ファインマンの熱ラチェットにおける，爪と歯止めの非対称な構造と両者の「温度差」に関して，キネシン－微小管系との対応関係を議論する．キネシンスーパーファミリーの一員であるncdは，キネシンとほぼ同じ立体構造のモータードメインをもちながらも，微小管のマイナス端方向に滑り運動を発生する．さらに，キネシンやncdのモータードメインの少数のアミノ酸残基を置換すると，運動方向が変調される例も報告されている[14)]．また，ATPの加水分解反応を伴わない場合は，キネシンに加える負荷が大きいほど，微小管から解離しやすくなり[15)]，式（2）とは矛盾する結果が得られている．以上のような実験事実は，微小管の方向性やキネシン－微小管系の分子構造によって，爪と歯止めの非対称性が一意に生み出されているわけではないことを示すものである．

次に，爪と歯止めに見られた2つの「温度」に関して，その物理的な意味を考えてみる．熱平衡の状態において，ある自由度のゆらぎの大きさ$\langle x^2 \rangle$は，エネルギー等分配則に従うので，

$$\frac{1}{2}K\langle x^2 \rangle = \frac{1}{2}k_BT' \qquad (3)$$

と記述できる．ここで，Kはバネ定数，k_BはBoltzmann定数，T'は「温度」である．今，仮に式（3）がタンパク質内部のある自由度に対して成立するならば，同じバネ定数Kのもとでは（爪と歯止めのモデルでは運動方向にかかわらず障壁の高さは同じ），構造のゆらぎ$\langle x^2 \rangle$の違いは，「温度」T'の違いとして検出されることになる．したがって，運動解析から求められた2つの「温度」とは，分子内部（キネシン－微小管複合体）の構造が非対称にゆらいでいるものと解釈できる．このゆらぎの非対称性は，ATPを加水分解することによって得られた自由エネルギーを用いて作り出されたのであろう．

それでは，爪と歯止めの「温度差」はどのようにして保持されているのだろうか？　溶媒中において，溶質分子は通常ピコ秒の時間領域で振動エネルギーを散逸させてしまうため，タンパク質がミリ秒以上の時間にわたって振動エネルギーの形で「高温状態」を維持するのは困難であろう．また，多くの色素は，蛍光を発することでエネルギーを放出させており，その蛍光寿命はナノ秒程度しかない．ところが，励起一重項状態から励起三重項状態へと項間交差が生じると，三重項状態か

ら基底状態への緩和は禁制遷移となるので，三重項状態はゆっくりと放射するエネルギーだめとして働くことになる．このゆっくりとしたエネルギー緩和過程は，リン光として観測される．興味深いことに，固体試料からのリン光は一般に明るく，その原因は，励起状態での非効率なエネルギー移動が項間交差を生じさせる確率を高くしている点にある．もしかしたら，タンパク質は，リン光現象に見られるようなゆっくりとしたエネルギー緩和過程を，複雑な立体構造を形成することで実現させているのかもしれない．キネシンは，どのようなメカニズムでファインマン型の熱ラチェットを達成しているのか，また，その物理的な意味はどこにあるのか，これらは実験家のみならず，理論家にとっても今後の大きな課題である．

5. むすび

本稿では，キネシンの1分子計測と両方向性ステップの運動解析を紹介してきた．ファインマンの熱ラチェット機構から示唆される分子モーターの動作原理とは，ATPの化学エネルギーが，分子の状態や分子間の相互作用を大きく変化させることで仕事を生み出すきわめてダイナミックなメカニズムであった．筆者らは，このファインマン型の熱ラチェット機構は，生体分子モーターのみならず，高分子の機能発現において本質的な役割を果たしていると考えている．

謝 辞

本研究の実験結果は，科学技術振興事業団1分子過程プロジェクトにて得られたものであり，大阪大学の柳田敏雄教授に深く感謝いたします．また，有益な議論をしていただきました大沢文夫先生にも御礼申し上げます．

文 献

1) 川口喜治，上村想太郎，石渡信一 (2002) 生物物理 42, 156-161.
2) Woehlke, G. and Schliwa, M. (2000) *Nature Reviews Molecular Cell Biology* 1, 50-58.
3) Svoboda, K., Schmidt, C. F., Schnapp, B. J. and Block, S. M. (1993) *Nature* 365, 721-727.
4) Kojima, H., Muto, E., Higuchi, H. and Yanagida, T. (1997) *Biophys. J.* 73, 2012-2022.
5) 西山雅祥 (2001) 光学 30, 445-450.
6) Kudo, S., Magariyama, Y. and Aizawa, S. (1990) *Nature* 346, 677-680.
7) Nishiyama, M., Muto, H., Inoue, Y., Yanagida, T. and Higuchi, H. (2001) *Nature Cell Biol.* 3, 425-428.
8) Nishiyama, M., Higuchi, H. and Yanagida, T. (2002) *Nature Cell Biol.* 4, 790-797.
9) 大沢文夫 (1998) 講座：生物物理 184-191, 丸善, 東京.
10) Feynman, R. P. (1963) ファインマン物理学 Vol.II, 岩波書店, 東京.
11) Reimann, P. (2002) *Phys. Rep.* 361, 57-265.
12) Nishiyama, M., Higuchi, H., Ishii, Y., Taniguchi, Y. and Yanagida, T. (2003) *Biosystems* 71, 147-158.
13) 徳永万喜洋 (1997) ナノピコスペースのイメージング (柳田敏雄, 石渡信一編) 130-157, 吉岡書店, 京都.
14) Higuchi H. and Endow, S. A. (2002) *Curr. Opin. Cell. Biol.* 14, 50-57.
15) Uemura S., Kawaguchi K., Yajima J., Edamatsu M., Toyoshima YY., Ishiwata, S. (2002) *Proc. Natl. Acad. Sci. USA.* 99, 5977-5981.

Available online at www.sciencedirect.com
SCIENCE DIRECT®
Chemical Physics Letters 385 (2004) 323–328
CHEMICAL PHYSICS LETTERS
www.elsevier.com/locate/cplett

Electronic properties of radial single-walled carbon nanotubes

Yoshinori Sato [a,*], Balachandran Jeyadevan [b], Rikizo Hatakeyama [a], Atsuo Kasuya [c], Kazuyuki Tohji [b]

[a] *Graduate School of Engineering, Tohoku University, Aoba 05 Aramaki Aoba-ku, Sendai 980-8579, Japan*
[b] *Graduate School of Environmental Studies, Tohoku University, Sendai 980-8579, Japan*
[c] *Center for Interdisciplinary Research, Tohoku University, Sendai 980-8578, Japan*

Received 15 December 2003; in final form 15 December 2003
Published online: 22 January 2004

Abstract

We investigated the electronic properties of the radial single-walled carbon nanotubes (SWCNTs) by using the Raman and the UV–Vis–NIR spectroscopy. The radial SWCNTs for the analysis were synthesized by the arc-discharge method with Ce as a catalyst. The yield of the radial SWCNTs with 1.55 nm diameter and 60 nm length was as high as 20% in the soot. From the UV–Vis–NIR spectrum and the tangential mode of Raman spectra, the radial SWCNTs were confirmed to be composed of semiconducting (0.64 and 1.14 eV for $V_s^1 \rightarrow C_s^1$ and $V_s^2 \rightarrow C_s^2$) and metallic (1.60 eV for $V_m^1 \rightarrow C_m^1$) nanotubes.
© 2004 Elsevier B.V. All rights reserved.

1. Introduction

The discovery [1,2], high-yield synthesis [3] and purification [4,5] of single-walled carbon nanotubes (SWCNTs) with novel properties have inspired scientists from various disciplines working on a range of potential applications [6–9]. Physical [10], chemical [11] and mechanical [12] properties of SWCNTs depend on their diameter, chirality and morphology. In the SWCNTs, there are two type morphologies; one is a tens of micrometer long SWCNTs, the so-called 'highway junction type SWCNTs' and the other is a tens of nanometer long radial SWCNTs, often referred to as 'sea urchin type SWCNTs'. Highway junction type SWCNTs have been synthesized by means of the arc-discharge method or the laser vaporization method using the bi-metal catalyst, Ni/Co, Ni/Fe, Ni/Y and Rh/Pd. Also, the optical properties of the highway junction type SWCNTs have been studied in detail and have been found to be composed of both semiconducting and metallic tubes [13,14]. On the other hand, radial SWCNTs with 1.5–2.0 nm in diameter and 50–100 nm in length are grown radially around the core metal particles. They have been synthesized by an arc-discharge [15–17] and solar focused production method [18] using a metal catalyst such as, Y, La, Ce and Gd. However, the production efficiency of the radial SWCNTs has been reported to be very low (roughly 6% by volume from visual inspection of TEM images [19]) and no detailed study has been carried out to improve the production efficiency. As a result, there is little or no information about their electronic properties [18,20]. Alvarez et al. [18,20] have synthesized the radial SWCNTs by the solar focused production method using La as a catalyst. They measured the Raman spectra of radial SWCNTs with diameters from 1.5 to 1.8 nm using the incident light energy of 1.92, 2.41 and 2.54 eV and reported that the tube possesses semiconducting character due to no Breit–Wigner–Fano (BWF) lineshape resonance. However, in order to investigate the metallic nature of these nanotubes, Raman spectroscopic measurement with laser energy close to 1.5 eV will be necessary and the electronic structure of the radial SWCNTs is yet to be clarified. Here, we discuss the parameters that need to be optimized for efficient production of radial SWCNTs by using the arc-discharge method with Ce as a catalyst. And also, we report their electronic structure by using Raman and UV–Vis–NIR spectroscopy.

* Corresponding author. Fax: +81-22-217-7391.
E-mail address: hige@bucky1.kankyo.tohoku.ac.jp (Y. Sato).

0009-2614/$ - see front matter © 2004 Elsevier B.V. All rights reserved.
doi:10.1016/j.cplett.2004.01.004

2. Experimental

Radial SWCNTs were synthesized by a direct current arc-discharge between a pure graphite cathode and a metal loaded graphite anode in helium atmosphere. A 16 mm diameter and 50 mm long pure graphite rod (purity 99.9%) and a 6 mm diameter and 85 mm long graphite rod (99.9%) loaded with CeO_2 powder (99.99%) as the source of Ce metal were used as cathode and anode, respectively. The soot samples were synthesized by varying the He gas (99.99%) pressure from 100 to 1500 Torr and the arc-discharge current from 60 to 100 A. The sample for the investigation was collected only from the inner wall of the chamber and burned in air at 533 K for 1 h to remove the amorphous carbon. Transmission electron microscope (TEM) (Hitachi HF-2000) with a field emission type electron gun was used to observe the morphology of the soot. Raman spectrometers, Jobin-Yvon T64000 with Ar ion (Leonix Co.) and He-Ne (NEC Co.) lasers and Jobin-Yvon LabRam HR-800 with diode laser (TOPTICA Photonics AG.), were used to analyze the physical properties of radial SWCNTs. Samples were measured using 488.0, 514.5, 632.8 and 785.0 nm exciting lasers under backscattering configuration. The UV–Vis–NIR spectrum of the radial SWCNTs thin film was measured with a Hitachi U-4100 spectrophotometer. The used film was prepared by the method described below. First, 10 mg of radial SWCNTs soot was ultrasonicated in 100 mL of butyl acetate to prepare a homogeneous dispersion. Finally, the suspension was sprayed on a quartz plate using an airbrush. Then, the film was dried at 473 K in vacuum (10^{-3} Torr) for 24 h to remove the butyl acetate absorbed on SWCNTs.

3. Results and discussion

Fig. 1a–c show the Raman intensity ratio I_G/I_D of the soot synthesized under a varying He gas pressure, arc current and Ce concentration, respectively. Here, the Raman spectra were measured using the incident light of 2.54 eV. Raman scattering peaks corresponding to E_{2g} vibration modes at 1568 and 1590 cm^{-1} in the tangential mode range were due to the zone folding effect of the SWCNTs. Since the peak at 1350 cm^{-1} is the Raman active mode of the defective carbon network, the intensity is roughly proportional to the amount of amorphous carbon in the sample. Therefore, the Raman intensity ratio I_G/I_D of the peaks at 1350 cm^{-1} (D-band) and 1590 cm^{-1} (G-band) is a good index for the evaluation of SWCNTs abundance. As seen in Fig. 1, the productivity of radial SWCNTs was very sensitive to He pressure and arc current for the soot synthesized with Ce concentration of about 1.7 at.%. In the arc-discharge, the temperature of the arc plasma changes by the gas pressure, arc-discharge current, or convection [21–23]. We suppose that the production of radial SWCNTs is influenced very much by the temperature distribution and its gradient around the arc plasma [24]. Thus, the optimum synthesis condition for a high yield of SWCNTs was found to be Ce concentration of 1.7 at.%, He pressure of 500 Torr and arc-discharge current of 70 A. We characterized the radial SWCNTs synthesized under the above condition.

Fig. 2 shows the typical low magnification TEM images of the soot synthesized under He gas pressures of (a) 100 Torr and (b) 500 Torr, while the Ce concentration in the anode and arc-discharge current were 1.7 at.% and 70 A, respectively. In the soot synthesized under the He pressure of 100 Torr, radial SWCNTs were not produced as seen in Fig. 2a. Also, most of the Ce metal nanoparticles were buried in spherical amorphous carbon particles. On the other hand, large quantities of radial SWCNTs were observed in the soot synthesized at the He pressure of 500 Torr. Fig. 2c is the high-resolution TEM image of the radial SWCNTs soot. From the TEM observation, it is found that the average diameter of SWCNTs was 1.6 nm in the range between 1.4 and 2.1 nm. The length was distributed between 50 and

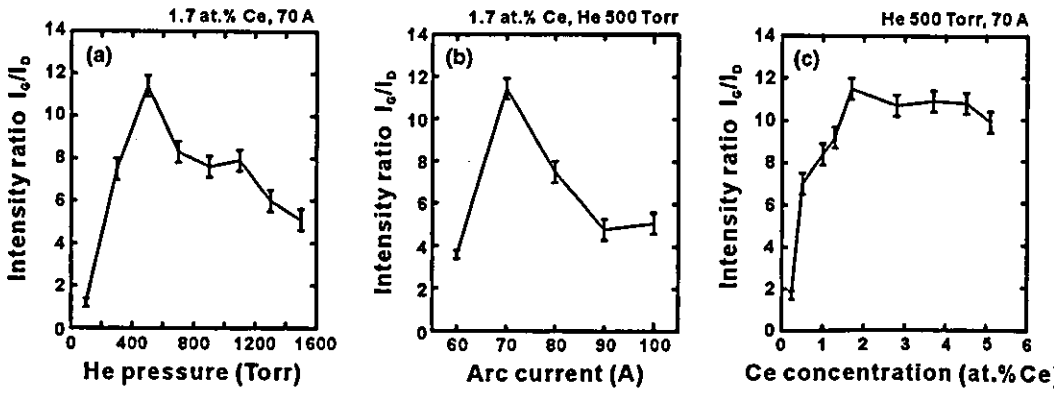

Fig. 1. The Raman intensity ratios I_G/I_D of the soot synthesized under varying: (a) He gas pressure; (b) arc current; (c) Ce concentration. Raman spectra were measured using the incident light of 2.54 eV.

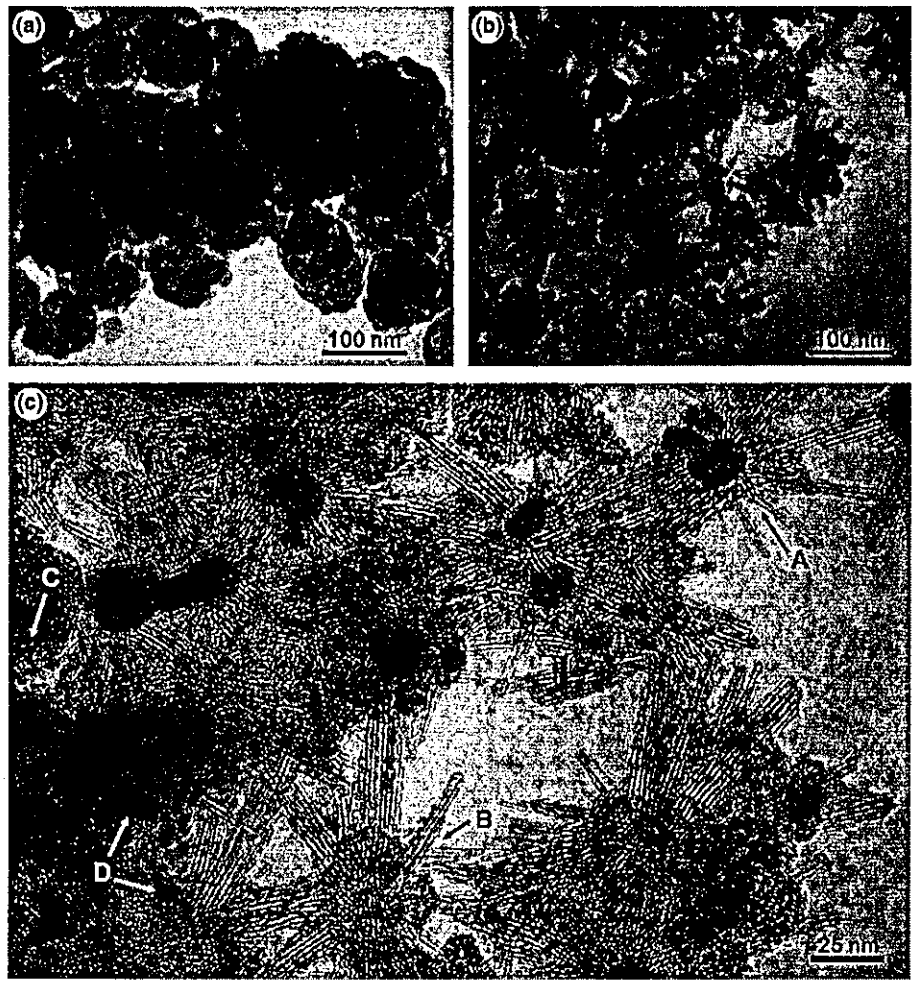

Fig. 2. Typical low magnification TEM images of the soot synthesized under a He gas pressure of (a) 100 Torr (b) 500 Torr while the Ce concentration in the anode and arc-discharge current were 1.7 at.% and 70 A, respectively. (c) A high-resolution TEM image of radial SWCNTs soot synthesized under a He gas pressure of 500 Torr shows (A) radial SWCNTs with Ce carbide metal particle at the core, (B) radial SWCNTs with small metal particles at the core, (C) amorphous carbons and (D) Ce carbide particles.

70 nm and was shorter than that of the highway junction type. The diameter of bundles grown from Ce compound core was not always uniform and but it varied between 5.0 and 16.0 nm. The soot consisted of (arrow A) radial SWCNTs with Ce carbide metal particle at the core, (arrow C) amorphous carbon and (arrow D) Ce carbide particles as shown in Fig. 2c. However, not all of the core metals can be formed in the radial SWCNTs; there are some radial SWCNTs with the aggregated small metal particles around the core as shown in arrow B. The yield of radial SWCNTs was estimated to be about 20% from the TEM observations.

Fig. 3a, b show the radial breathing mode (RBM) and tangential mode (TM) ranges of Raman spectra using exciting laser with various photon energies for the soot synthesized at Ce concentration of 1.7 at.%, He pressure of 500 Torr and arc-discharge current of 70 A and subsequently burned in air at 533 K for 1 h. As shown in Fig. 2, the radial SWCNTs were self-assembled into bundles and the diameter distribution of radial SWCNTs was determined from the Raman line in RBM range using the equation

$$\nu(\mathrm{cm}^{-1}) = 223.5(\mathrm{cm}^{-1}\mathrm{nm})/d(\mathrm{nm}) + 12.5$$

derived from the van der Waals interaction of the nanotube packing [25]. To suppress the resonant Raman effect, an incident light with photon energy of 2.54 eV was used along with 2.41 eV [14]. From the peaks at 149 and 159 cm^{-1}, the mean diameter of the radial SWCNTs was estimated to be about 1.55 nm. These results were in good agreement with the diameter observed from the TEM images. In the profiles obtained by using the incident lights of 1.96, 2.41 and 2.54 eV in the TM range, the peak often observed in graphite at 1580 cm^{-1}, split into two peaks with their peak positions at 1570 and 1590 cm^{-1}. On the other hand, in the Raman spectrum measured using the incident light of 1.57 eV, a strong peak at 1588 cm^{-1} followed by a weak one at 1566 cm^{-1}

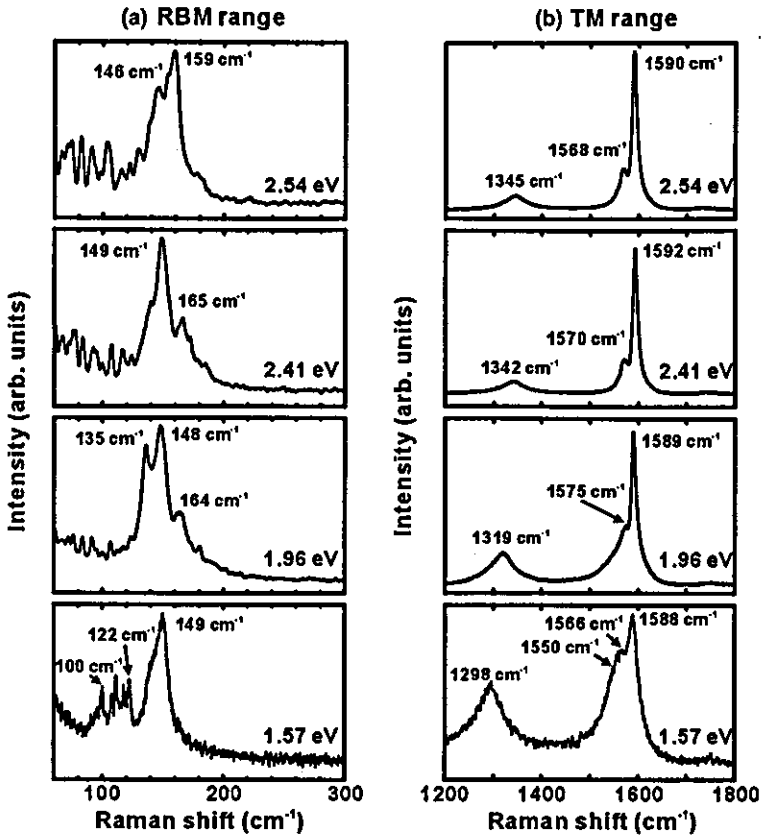

Fig. 3. Raman spectra in (a) RBM and (b) TM ranges using exciting laser with various photon energies for the soot synthesized at Ce concentration of 1.7 at.%, He 500 Torr and arc-discharge current of 70 A and subsequently burned in the air at 533 K for 1 h.

and a shoulder around 1550 cm^{-1} was observed. According to the relationship between diameter and the allowed optical transitions (transfer integral 2.9 eV) derived from band structure calculation based on the tight binding approximation [13,26], a SWCNT with a diameter of 1.5–1.6 nm will be exited by the incident light with energies 1.96, 2.41 and 2.54 eV only when the nanotube is a semiconductor. On the other hand, the metallic nanotube will be exited by an incident light of 1.57 eV. In the TM range, the shape of Raman spectra depends on the laser energy [27–29] and the splitting of the spectra into narrow and symmetric lines is assigned to the resonance from semiconducting SWCNTs, while the broad and asymmetric BFW lineshape type peak [13,30] that centered around 1550 cm^{-1} was assigned to the resonance from the metallic SWCNTs. Therefore, the broad lineshape around 1550 cm^{-1} was due to the presence of metallic SWCNTs.

UV–Vis–NIR spectroscopy is an established technique for characterizing the electronic band structure of SWCNTs [13,14,31–34]. Fig. 4 shows the UV–Vis–NIR spectrum of the soot synthesized at a Ce concentration of 1.7 at.%, He gas pressure of 500 Torr and arc-discharge current of 70 A and subsequently burned in air at 533 K for 1 h. The three peaks at 0.64, 1.14 and 1.60 eV were identified after the strong background due to π electron plasmon of two-dimensional carbon was subtracted from the raw data (inset in Fig. 4). By comparing the peak positions with the values calculated based on the zone folding method [26], these features

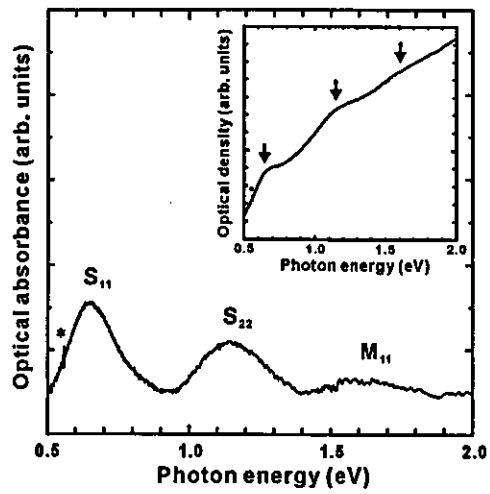

Fig. 4. UV–Vis–NIR spectrum of the soot synthesized at Ce concentration of 1.7 at.%, He 500 Torr and arc-discharge current of 70 A and subsequently burned in the air at 533 K for 1 h. Inset shows the raw UV–Vis–NIR spectrum. Asterisk (*) indicates absorption peak due to the quartz substrate.

were assigned to the allowed optical transitions (transfer integral 2.9 eV) between Van Hove singularities of the density of states in the SWCNT with a diameter of 1.5–1.6 nm. The peaks at 0.64 and 1.14 eV were attributed to the electronic transitions between pairs of singularities in semiconducting SWCNTs ($V_s^1 \rightarrow C_s^1$ and $V_s^2 \rightarrow C_s^2$, respectively), whereas the peak at about 1.60 eV was predominantly from the first pair of singularities ($V_m^1 \rightarrow C_m^1$) in metallic SWCNTs. The appearance of the absorbed energy of the M_{11} band appears at about 1.60 eV confirmed the presence of metallic SWCNTs. This result was in good agreement with the electronic band structure of SWCNTs measured from the Raman scattering spectra. The reason for its appearance at a higher-energy side compared to the calculated S_{11} is due to the Coulomb interaction between SWCNTs [35].

4. Conclusion

We have succeeded in improving the production efficiency of the radial SWCNTs to a value as high as about 20% (by volume from visual inspection of TEM images) using 1.7 at.% of Ce in anode, He gas pressure of 500 Torr and arc-discharge current of 70 A. From the TEM measurement and radial breathing mode of Raman spectra, the average length and diameter of the SWCNTs were determined to be 60 and 1.55 nm, respectively. Also, we have clarified the nature of the electronic structure of the radial SWCNTs. The presence of the metallic and semiconductor type SWCNTs was confirmed from the UV–Vis–NIR spectrum and the tangential mode of Raman spectra. In the carbon materials, conducting amorphous carbon has played an important role on the composites such as the electrode, conducting paints and conducting rubber. The nanotube-filler used in these applications is required to be conducting and easy to disperse in polymer and the nanotubes could be used to form the conducting channel within the polymer. The radial SWCNTs are more easily dispersed in polymer than the semi-finite long SWCNTs. We believe that the radial SWCNTs are applied as the conducting filler.

Acknowledgements

This work was supported by Grant-in-Aid for Basic Research #(S) 14103016 and #(S) 13852016 from the Ministry of Education, Science, Culture and Sport of Japan and #H14-nano-021 from the Ministry of Health, Labor and Welfare. The authors thank Mr. K. Motomiya of Tohoku University, Dr. T. Kamino and Dr. T. Yaguchi of Hitachi Science Systems, Ltd. for their assistance in HRTEM analysis. Y. S. thanks Dr. T. Takenobu of Institute for Materials Research, Tohoku University for useful information and Prof. A. Narayanasamy of University of Madras and Dr. C. N. Chinnasamy of Tohoku University for useful discussion. Also, the authors thank Dr. T. Kochi and Dr. S. Okamoto of HORIBA, Ltd. for the measurement of Raman scattering spectrum and Dr. Yamada of Hitachi Science Systems, Ltd. for the measurement of UV–Vis–NIR spectrum.

References

[1] S. Iijima, T. Ichihashi, Nature 363 (1993) 603.
[2] D.S. Bethune, C.H. Kiang, M.S. de Vries, G. Gorman, R. Savoy, J. Vazquez, R. Beyers, Nature 363 (1993) 605.
[3] A. Thess, R. Lee, P. Nikolaev, H. Dai, P. Petit, J. Robert, C. Xu, Y.H. Lee, S.G. Kim, A.G. Rinzler, D.T. Colbert, G.E. Scuseria, D. Tománek, J.E. Fischer, R.E. Smalley, Science 273 (1996) 483.
[4] K. Tohji, T. Goto, H. Takahashi, Y. Shinoda, N. Shimizu, B. Jeyadevan, I. Matsuoka, Y. Saito, A. Kasuya, T. Ohsuna, K. Hiraga, Y. Nishina, Nature 383 (1996) 679.
[5] J.L. Andrew, G. Rinzler, H. Dai, J.H. Hafner, R.K. Bradley, P.J. Boul, A. Lu, T. Iverson, K. Shelimov, C.B. Huffman, F. Rodriguez-Macias, Y.S. Shon, T.R. Lee, D.T. Colbert, R.E. Smalley, Science 280 (1998) 1253.
[6] R.H. Baughman, A.A. Zakhidov, W.A. de Heer, Science 297 (2002) 787.
[7] S.J. Tans, M.H. Devoret, H. Dai, A. Thess, R.E. Smalley, L.J. Geerligs, C. Dekker, Nature 386 (1997) 474.
[8] H. Dai, Acc. Chem. Res. 35 (2002) 1035.
[9] A. Modi, N. Koratkar, E. Lass, B. Wei, P.M. Ajayan, Nature 424 (2003) 171.
[10] R. Saito, G. Dresselhaus, M.S. Dresselhaus, Physical Properties of Carbon Nanotubes, Imperial College Press, London, 1998.
[11] S. Niyogi, M.A. Hamon, H. Hu, B. Zhao, P. Bhowmik, R. Sen, M.E. Itkis, R.C. Haddon, Acc. Chem. Res. 35 (2002) 1105.
[12] M.F. Yu, B.S. Files, S. Arepalli, R.S. Ruoff, Phys. Rev. Lett. 84 (2000) 5552.
[13] H. Kataura, Y. Kumazawa, Y. Maniwa, I. Umezu, S. Suzuki, Y. Ohtsuka, Y. Achiba, Synth. Met. 103 (1999) 2555.
[14] H. Kuzmany, W. Plank, M. Hulman, C. Kramberger, A. Grüneis, T. Pichler, H. Peterlik, H. Kataura, Y. Achiba, Eur. Phys. J. B 22 (2001) 307.
[15] S. Subramoney, R.S. Ruoff, D.C. Lorents, R. Malhotra, Nature 366 (1993) 637.
[16] D. Zhou, S. Seraphin, S. Wang, Appl. Phys. Lett. 65 (1994) 1593.
[17] Y. Saito, K. Kawabata, M. Okuda, J. Phys. Chem. 99 (1995) 16076.
[18] L. Alvarez, T. Guillard, J.L. Sauvajol, G. Flamant, D. Laplaze, Appl. Phys. A 70 (2000) 169.
[19] A. Kasuya, Y. Sasaki, Y. Saito, K. Tohji, Y. Nishina, Phys. Rev. Lett. 78 (1997) 4434.
[20] L. Alvarez, A. Righi, T. Guillard, S. Rols, E. Anglaret, D. Laplaze, J.L. Sauvajol, Chem. Phys. Lett. 316 (2000) 186.
[21] C.G. Suits, J. Appl. Phys. 10 (1939) 728.
[22] W. Finkelnburg, J. Appl. Phys. 20 (1949) 468.
[23] A.L. Phillips (Ed.), Welding Handbook, sixth ed., American Welding Society, New York, 1968 (Sec.1, Chapter 3).
[24] L. Alvarez, T. Guillard, J.L. Sauvajol, G. Flamant, D. Laplaze, Chem. Phys. Lett. 324 (2001) 7.
[25] S.M. Bachilo, M.S. Strano, C. Kittrell, R.H. Hauge, R.E. Smalley, R.B. Weisman, Science 298 (2002) 2361.
[26] S.D.M. Brown, P. Corio, A. Marucci, M.A. Pimenta, M.S. Dresselhaus, G. Dresselhaus, Phys. Rev. B 61 (2000) 7734.

[27] A. Kasuya, M. Sugano, T. Maeda, Y. Saito, K. Tohji, H. Takahashi, Y. Sasaki, M. Fukushima, Y. Nishina, C. Horie, Phys. Rev. B 57 (1998) 4999.
[28] M. Sugano, A. Kasuya, K. Tohji, Y. Saito, Y. Nishina, Chem. Phys. Lett. 292 (1998) 575.
[29] M.A. Pimenta, A. Marucci, S.A. Empedocles, M.G. Bawendi, E.B. Hanlon, A.M. Rao, P.C. Eklund, R.E. Smalley, G. Dresselhaus, M.S. Dresselhaus, Phys. Rev. B 58 (1998) 16016.
[30] Z. Yu, L. Brus, J. Phys. Chem. B 105 (2001) 1123.
[31] J. Chen, M.A. Hamon, H. Hu, Y. Chen, A.M. Rao, P.C. Eklund, R.C. Haddon, Science 282 (1998) 95.
[32] M.E. Itkis, S. Niyogi, M.E. Meng, M.A. Hamon, H. Hu, R.C. Haddon, Nano Lett. 2 (2002) 155.
[33] P. Petit, C. Mathis, C. Journet, P. Bernier, Chem. Phys. Lett. 305 (1999) 370.
[34] S. Kazaoui, N. Minami, R. Jacquemin, H. Kataura, Y. Achiba, Phys. Rev. B 60 (1999) 13339.
[35] M. Ichida, S. Mizuno, Y. Tani, Y. Saito, A. Nakamura, J. Phys. Soc. Jpn. 68 (1999) 3131.

Journal of the Physical Society of Japan
Vol. 72, No. 9, September, 2003, pp. 2224–2228
©2003 The Physical Society of Japan

Electronic States of $SnBr_4$ Single Crystal and of Its Clusters Inserted in the Molecular Vessel of Cyclodextrin

Chang Jun YE, Bold GOMBOJAV, Takehisa YOSHINARI*, Shin-ichiro NAGASAKA, Yoshio TAKAHASHI, Aishi YAMAMOTO[1†], Takenari GOTO[2] and Atsuo KASUYA[3]

Department of Physics, Faculty of Science, Yamagata University, Kojirakawa, Yamagata 990-8560
[1]*Department of Physics, Graduate School of Science, Tohoku University, Sendai 980-8578*
[2]*Organo-Optic Research Laboratory, 6-2-1 Seiwa-dai, Kita-ku, Kobe 651-1121*
[3]*Center for Interdisciplinary Research, Tohoku University, Sendai 980-8578*

(Received May 14, 2003)

The dry powder vessels of cyclodextrin including tin tetrabromides, $SnBr_4$ were prepared in vacuum to investigate the electronic states of the isolated molecule. From the reflection spectra of $SnBr_4$ single crystal, the exciton absorption band has been observed at peak energies 3.64 eV (2 K) and 3.21 eV (room temperature). The reflection spectra of $SnBr_4$ clusters inserted in α-, β- and γ-cyclodextrins were measured. The lowest energy absorption peak of the molecule shows broad absorption band in 3–6 eV. It is analyzed as the overlapped shape of two absorption bands which are separated about 0.5 eV. They come from the spin–orbit split of HOMO state which is made of bromines and $5sp^3$ mixed states of a tin.

KEYWORDS: tin tetrabromide, $SnBr_4$, cluster, single crystal, cyclodextrin, optical absorption spectra, spin–orbit interaction
DOI: 10.1143/JPSJ.72.2224

1. Introduction

Cyclodextrin (CyD) is a cylindrical organic compound. It is possible to insert various kinds of materials such as anthracene, pyrene, thiophene in it.[1)] We have reported on the optical properties of the cluster state of tin tetraiodides, SnI_4 by inserting them in a CyD. The optical spectra of SnI_4 single crystal show the exciton absorption band. The spin–orbit split pair of the exciton absorption band could not be clarified in the spectra of the single crystal. In the optical spectra of a single molecule, it was observed that the absorption band had two separated peaks with 0.8 eV. The energy is close to the spin–orbit interaction energy. SnI_4 is easy to deal with it experimentally, because the melting temperature is high as 417.7 K and the single crystal is not hygroscopic.[2,3)]

On the other hand, there are only a few papers on tin tetrabromide, $SnBr_4$ which is the similar inorganic compound SnI_4. Almost all the papers reported on the crystal structure of $SnBr_4$.[4–6)] Only one paper shows the optical absorption spectra of $SnBr_4$ vapor.[7)] It is quite difficult to deal with the $SnBr_4$ single crystals experimentally, because of its low melting temperature, 304 K and of the very high hygroscopic property. Although the fresh single crystal is transparent, its surface quickly becomes opaque white in the experimental atmosphere like sodium iodide crystal. It should be dealt in dry nitrogen gas flow for optical measurements.

The main purpose of this paper is to clarify the energy levels of tin halide compounds. The single molecule of tin tetrabromide, $SnBr_4$, was settled inside the CyD molecules in the present study by the same way as the SnI_4.

The electronic configuration of the neutral tin atom is $[Kr]4d^{10}5s^25p^2$, where [Kr] represents the electronic configuration of the rare gas krypton atom. The sp^3 hybrid orbital in a tin atom makes four equivalent bonding hands, while the configuration of bromine is $[Ar]3d^{10}4s^24p^5$. Four bromines are bound to a tin atom by the covalent bonds. Then, the $SnBr_4$ forms a tetrahedral molecule similar to a methane. The cohesion of neutral $SnBr_4$ molecules is due to the van der Waals force. The electron affinity of bromine is stronger than iodine, thus the bromines are more negatively charged than iodines in SnI_4. The bromines of $SnBr_4$ molecules are nearly close-packed in the crystal and are weakly charged negative. This is the origin of the low melting temperature, 304 K under atmospheric pressure.

Table I. Physical characters of α-, β- and γ-CyD's.

	Number of glucoses	Molecular weight	Inner diameter D (nm)	Depth d (nm)
α-CyD	6	972	0.45	0.70
β-CyD	7	1135	0.70	0.70
γ-CyD	8	1297	0.85	0.70

The crystal structure of $SnBr_4$ is monoclinic and the space group is $P2_1/c$. There are four $SnBr_4$ molecules in the unit cell. Bromine atoms of nearest neighbor molecules are in nearly the close-packed, and the tin atoms occupy the center of four bromine atoms in each molecule.[4–6)]

The numerical values of CyD are summarized in Table I.[1)] Their inner diameter are at the center of the tubes.

2. Experimental

2.1 *Single crystal of $SnBr_4$*

Single crystals of $SnBr_4$ were made by vapor growth method from the commercial product of $SnBr_4$ powder. The powder purity is 99%. The melting point is 304 K and the boiling point is 480 K. Hard glass tube (borosilicate glass) was washed by filling it with nitric acid for half a day and washed four times with distilled water using ultrasonic washer for twenty minutes of each times. The glass tube was dried, and the inside was evacuated for five hours at 593 K.

*E-mail: tak@sci.kj.yamagata-u.ac.jp
†Present address: Graduate School of Materials Science, Nara Institue of Science and Technology, Takayama 8916-5, Ikoma, Nara 630-0192.

Then the glass tube was cooled to RT and filled with argon gas. The molecular weight of argon is 39, which is heavier than that of air, 29. The glass tube was taken off from the evacuation system by holding the open edge upward, and then the open edge was quickly covered with a thin paraffin film (Parafilm). The $SnBr_4$ powder was quickly put into the glass tube and then covered again with the film. In these treatments, humid air did not come into the glass tube, because the tube was filled with argon gas, which is heavier than air. The glass tube was again set to the vacuum system and evacuated for five minutes and then filled with argon gas again. This treatment was done five times. Then, it was evacuated again with a diffusion pump to 1.3×10^{-3} Pa, and the glass tube was sealed with gas flame. In this evacuation process two liquid nitrogen traps were inserted between the glass tube and the pumps to prevent the contamination of the pump oil.

The glass tube was kept at 278 K for four weeks in a refrigerator. Transparent $SnBr_4$ crystals were grown inside the glass tube. The glass tube was broken, and the crystals were taken out from the tube and then again put into a newly prepared glass tube and treated as the same way mentioned above. Recrystallized pure grade crystals were used for optical reflection measurements.

The size of $SnBr_4$ single crystals for optical measurements was $10 \times 10 \times 5\,mm^3$. Single crystal is transparent at RT. Big size crystals are not good for optical measurements, because they are more hygroscopic than small size crystals. Since the bigger size crystals may be polycrystals, they have small voids among domains of the crystals and the humid air may not completely be taken off by the evacuation. Thus, they easily loose the luster of the crystal surfaces.

The single crystals were taken out from the glass tube by breaking it in a dry box. Dry nitrogen gas was constantly flown by evaporating liquid nitrogen with a heater. The temperature inside the dry box was kept lower than 283 K with the cool nitrogen gas by controlling the heater voltages. Crystals were fixed on a finger of a long thin rod. While the rod was pulled out from the dry box, the sample holder part was covered with thin vinyl bag filled with dry and cold nitrogen gas. The rod was put into the entrance tube of a cooling dewar and slowly pushed down to the liquid helium surface and soaked into it. The crystal surfaces do not loose their luster by these treatments. Then the liquid helium was evacuated to 2 K by rotary pump in order to prevent the bubble noise for optical measurements.

The reflection spectra of the $SnBr_4$ single crystals were measured at RT, 77 K and 2 K. A deuterium lamp (Hamamatsu Photonics L1626, 24 W) was used for the light source to measure optical spectra in the wavelength region from 190 to 350 nm and a tungsten lamp (Ushio 12 V, 50 W) from 350 to 900 nm. Two sets of a monochromator (Acton Research Corporation Spectra Pro-500) with a CCD photodetector and that with a photodiode array (Hamamatsu Photonics C4448-11) system were used for the reflection measurements.

Room temperature (280 K) measurements were proceeded in the small dry box that has a fused quartz window. Dry and cool nitrogen gas was constantly flown in the box by evaporating liquid nitrogen with a heater as mentioned above.

2.2 *Sample preparation for $SnBr_4$ cluster in CyD and measurements*

Cleaned glass tubes were prepared as the same way mentioned above to make a cluster state of $SnBr_4$. They were evacuated, heated and filled with argon gas. The powder of CyD was put into the bottom of a glass tube and evacuated again. It was evacuated to 1.3×10^{-1} Pa with a rotary pump and to 1.3×10^{-3} Pa with a diffusion pump for one hour, and then heated and evacuated for nine hours. The heating temperatures were 413 K for α- and γ-CyD and 393 K for β-CyD. The glass tube was cooled to RT after it was heated, and the glass tube was filled with argon gas.

$SnBr_4$ single crystals were put into these glass tubes, in which CyD powder had already been put just mentioned above. This procedure had been done in the cooled dry box. Glass tube which contains CyD powder and $SnBr_4$ single crystals was evacuated for 10 min and then filled with argon gas. This treatment was done twice and the glass tube was evacuated to 1.3×10^{-3} Pa and then sealed.

The sealed glass tube was put in a heating glass tube that was wound with tungsten heater. It was heated at 300 K for a day and then one of the sealed tube edges was pulled out of the heating tube and kept for three hours in order to take off the excess $SnBr_4$ from the CyD powder surface. Excess $SnBr_4$ were recrystallized at the cooled edge. After then the sample tube was taken out from the heating tube. It is quickly put in a dried and cooled box.

The reflection spectra of the $SnBr_4$ clusters in CyD were measured by the following method. The $SnBr_4$ clusters in CyD were taken out by breaking the glass tube and were quickly pressed with a glass plate on the both-sided adhesive tape which was fixed to the finger of the sample holding rod. These treatments were also done in the dried and cooled box. The holder was soaked into liquid helium or liquid nitrogen using a glass dewar. Room temperature (at around 280 K) measurements were proceeded in the small dry box that had a fused quartz window. The dry and cool nitrogen gas was constantly flown in the box by evaporating liquid nitrogen with heater as mentioned above.

2.3 *Experimental results*

The reflection spectra of a $SnBr_4$ single crystal were measured at 2 K, 77 K and RT. The reflectivities were corrected by the absolute reflectivity measured with a He–Ne laser and an S1335-8BQ photodiode (Hamamatsu Photonics R955) at 632.8 nm, which is the transparent wavelength of $SnBr_4$ single crystal. The absolute reflectivity is about 5% at 632.8 nm (1.96 eV) at RT and also at 2 K. The absorption coefficients were calculated by the Kramers–Kronig formula. Since the reflectivity in the higher energy range than 6.2 eV could not be measured, they were extrapolated with the damping factor δ as $E^{-\delta}$, where E is photon energy. The criteria of fitting the parameter δ are as follows; the low energy side of exciton absorption damps to zero; the absorption coefficient is nearly zero in the transparent wavelength region. If the parameter was set incorrectly, some parts of the absorption coefficients became negative. The value δ was adjusted to be 1.5 to obtain a reasonable spectrum. The calculated absorption spectra are shown in Fig. 1. The exciton absorption band peak is at 3.64 eV at 2 K. It shifts to 3.59 eV at 77 K and to 3.21 eV at